RSC Advances

ROYAL SOCIETY OF CHEMISTRY

PAPER

View Article Online
View Journal | View Issue

Cite this: *RSC Adv.*, 2018, **8**, 20157

The enhancement of photocatalytic performance of $SrTiO_3$ nanoparticles *via* combining with carbon quantum dots†

Haitao Ren, Lin Ge, Qian Guo, Lu Li, Guangkuo Hu and Jiangong Li*

Received 9th March 2018
Accepted 17th May 2018

DOI: 10.1039/c8ra02103a

rsc.li/rsc-advances

Carbon quantum dots were prepared by a simple chemical process using activated carbon as carbon source. The as-prepared carbon quantum dots are fine with a narrow size distribution and show excellent hydrophilicity. The carbon quantum dots were combined with $SrTiO_3$ nanoparticles through a simple impregnation process to obtain a carbon quantum dots/$SrTiO_3$ nanocomposite. The photocatalytic reaction rate of carbon quantum dots/$SrTiO_3$ nanocomposite is about 5.5 times as large as that of pure $SrTiO_3$ in the degradation of rhodamine B under sunlight irradiation. The enhanced performance in the degradation of rhodamine B may be attributed to the interfacial transfer of photogenerated electrons from $SrTiO_3$ to carbon quantum dots, leading to effective charge separation in $SrTiO_3$. Carbon quantum dots show potential applications in high-efficiency photocatalyst design.

1. Introduction

Carbon quantum dots (CQDs) are a new type of carbon nanomaterials and have been drawing much attention in recent years due to their unique photoluminescence (PL), high chemical inertness, good hydrophilicity, low toxicity, good biocompatibility, environmental friendliness, and high photostability.[1–4] CQDs have shown promising applications in sensing,[5] drug delivery,[6] optoelectronic devices,[7] and bioimaging.[8] In addition, due to their excellent electron transfer and reservoir properties,[2,9] CQDs were used to enhance the photocatalytic performance of In_2S_3,[10] WO_3,[11] Bi_2SiO_5,[12] Ag_3PO_4,[13] $BiVO_4$,[14] Bi_2MoO_6,[15] Fe_2O_3,[16] and TiO_2.[17] Among various semiconductors, perovskite metal oxides such as $SrTiO_3$ are promising photocatalysts because of their excellent electronic and optical properties, photochemical stability, low cost, and high catalytic efficiency.[18] $SrTiO_3$ has been extensively studied for photodegradation of organic pollutants and water splitting.[19,20] However, the high electron (e^-) and hole (h^+) recombination efficiency of $SrTiO_3$ results in low photocatalytic performance.[21] Hence suppressing the e^- and h^+ recombination in $SrTiO_3$ is the key to enhance its photocatalytic performance. Therefore, we combine CQDs with $SrTiO_3$ to fabricate a novel CQD/$SrTiO_3$ nanocomposite to achieve the efficient separation of the photogenerated e^-–h^+ pairs and to enhance the photocatalytic performance.

To date, numerous processes including acidic oxidation,[22] ultrasonic treatment,[23] microwave treatment,[24] electrochemical exfoliation,[25] laser ablation,[26] thermal decomposition,[27] hydrothermal treatment,[28] plasma treatment,[29] and high-energy ball milling[30] have been developed to prepare CQDs from a variety of carbon precursors. Most of these processes suffer more or less from expensive precursor materials, complicated apparatus, harsh reaction conditions, tedious purification procedures, and high cost. Among these processes, acidic oxidation is an effective process for the large-scale preparation of carbon nanoparticles. Nevertheless, this process requires the neutralization of residual acid with a strong alkali. This results in a large amount of inorganic salt ions in the products and requires a tedious purification procedure.[31,32] Here we present a simple process to prepare CQDs by acidic oxidation of activated carbon with the most affordable oxidant, nitric acid (HNO_3). In our present work, the residual acid was directly evaporated rather than neutralized with a strong alkali. Thus the as-prepared CQDs contain no inorganic salt ions so that the purification procedure is simpler. Compared with other processes, our process is simple because no expensive reagents, no tedious purification procedures, no harsh reaction conditions, or no complicated apparatus are required.

The as-prepared CQDs are fine in size and have oxygen-containing functional groups (OCFGs) on their surface which endow them excellent hydrophilicity and facilitate further functionalization and applications. A novel nanocomposite photocatalyst (CQD/$SrTiO_3$) was fabricated by combining the as-prepared CQDs with $SrTiO_3$ nanoparticles through a simple impregnation process. Its photocatalytic performance was evaluated by degradation of Rhodamine B (RhB) under sunlight irradiation. Compared with pure $SrTiO_3$, the CQD/$SrTiO_3$

Institute of Materials Science and Engineering, Lanzhou University, Lanzhou 730000, China. E-mail: lijg@lzu.edu.cn

† Electronic supplementary information (ESI) available. See DOI: 10.1039/c8ra02103a

nanocomposite shows an excellent photocatalytic performance in the photodegradation of RhB. The photocatalytic reaction rate of the CQD/$SrTiO_3$ nanocomposite is about 5.5 times as large as that of pure $SrTiO_3$. Furthermore, the possible mechanism for the excellent photocatalytic performance of the CQD/$SrTiO_3$ nanocomposite will be discussed.

2. Experimental

2.1 Materials

Nitric acid was obtained from Xilong Chemical Co. Ltd (Shantou, China). Charcoal activated and rhodamine B were from Sinopharm Chemical Reagent Co. Ltd (Shanghai, China). Strontium nitrate and citric acid were provided by Kermel Chemical Reagent Co. Ltd (Tianjin, China). Titanium isopropoxide and ethylene glycol were purchased from Li'anlong Bohua Pharmaceutical Chemical Co. Ltd (Tianjin, China). All chemical reagents used in this work were analytical grade and used without further purification.

2.2 Instrumentation

Transmission electron microscopy (TEM) observations as well as selected-area electron diffraction (SAED) analysis were performed on an FEI Tecnai G^2 F30 field emission electron microscope operating at a voltage of 300 kV. X-Ray Diffraction (XRD) patterns (2θ scans) were recorded using a Rigaku D/Max-2400 X-ray diffractometer with Cu K_α radiation. Fourier transform infrared (FTIR) spectra were collected in the KBr medium on a Nicolet NEXUS 670 FTIR spectrometer. X-Ray Photoelectron Spectroscopy (XPS) measurements were performed on a Kratos Axis Ultra DLD spectrometer using Al K_α X-ray beam of 250 W as the excitation source. Scanning electron microscopy (SEM) observations and energy dispersive X-ray spectroscopy (EDS) analysis were conducted on a Hitachi S-4800 field emission scanning electron microscope working at an acceleration voltage of 20 kV. The diffuse reflectance ultraviolet-visible (UV-vis) absorption spectrum was measured using a Hitachi U-3900H spectrometer, and $BaSO_4$ was used as a reference standard. Electrochemical impedance spectra (EIS) were recorded on a RST5200 electrochemical work station with a three-electrode system at room temperature. The PL spectra were measured using an Edinburgh Instruments FLS920 spectrometer. The total organic carbon (TOC) analysis was conducted using a Shimadzu TOC-VCPH analyzer. Centrifugation was performed on a TG 22 centrifuge with rotation speeds tunable from 100 to 22 000 revolutions per minute (rpm).

2.3 Preparation of CQDs

For a typical process, 2.0 g activated carbon was added to 250 mL HNO_3 aqueous solution (3 mol L^{-1}). After 30 min ultrasonic bath, the mixture was refluxed for 16 h. The resulting mixture was cooled to room temperature and filtered. After the residual acid was completely evaporated at 80 °C in a water bath, light brown powders were obtained. The powders were dispersed in deionized water (60 mL), yielding a suspension containing CQDs. The suspension was centrifuged at 15 000 rpm for 10 min. Finally, a transparent, light brown supernatant containing CQDs was obtained.

2.4 Preparation of $SrTiO_3$ nanoparticles and CQD/$SrTiO_3$ nanocomposite

$SrTiO_3$ nanoparticles were prepared according to a reported process.[19] Typically, 3.26 mL titanium isopropoxide was dissolved in 25 mL ethylene glycol for about 30 min under an Ar atmosphere at room temperature. Then 20.82 g citric acid was added into the solution and stirred until complete dissolution of the reagents. Then 5.69 g strontium nitrate was slowly added into the solution under stirring until the solution became transparent. The solution was heated to about 120 °C and kept for 5 h to promote polymerization. After heating and evaporation of the solvents, the reaction mixture gelled into a transparent brown resin. The resin was charred at 350 °C for 3 h and cooled to room temperature. Subsequently, the charred resin was ground to fine powders. The obtained powders were calcined at 800 °C for 6 h. The calcined powders were washed three times with 2 mol L^{-1} HNO_3 aqueous solution and three times with deionized water and then dried in an oven at 80 °C for 12 h. Finally, $SrTiO_3$ nanoparticles were obtained.

CQD/$SrTiO_3$ nanocomposite was prepared *via* a simple impregnation process. In the experiments, CQD suspensions with a concentration of 0.75 mg mL^{-1} were obtained by suspending 15 mg CQDs in 20 mL deionized water. 0.06 g $SrTiO_3$ nanoparticles were added into 6 mL CQD suspension and mixed by stirring for 2 h. Then the mixture was dried in a vacuum oven at 80 °C for 12 h to obtain CQD/$SrTiO_3$ nanocomposite.

2.5 Photocatalytic measurements

In the experiments, 50 mg photocatalyst was suspended in 100 mL quartz silica glass beaker containing 50 mL RhB solution with a concentration of 10 mg L^{-1}. A 350 W high pressure Xe lamp was used for illumination to provide an artificial sunlight. The distance between the light source and samples was about 14 cm. Before irradiation, the suspension was magnetically stirred in dark for 30 min to achieve the adsorption/desorption equilibrium between photocatalyst and RhB. Then the suspension was irradiated under the artificial sunlight with continuous stirring. To analyze the concentration change of RhB, 5 mL suspension was sampled every 20 min and centrifuged (15 000 rpm, 5 min) to remove the solid photocatalysts ($SrTiO_3$ nanoparticles or CQD/$SrTiO_3$ nanocomposite). The concentration of RhB was determined from the absorbance at the wavelength of 554 nm using a PERSEE TU-1810 UV-vis spectrophotometer.

3. Results and discussion

3.1 Characterizations of CQDs

The morphology and structure of the CQDs prepared from activated carbon were analyzed by TEM and FTIR. The TEM image in Fig. 1a reveals that the as-prepared CQDs are completely disperse without any agglomeration, fine in size, and nearly spherical in shape. According to their size distribution histogram in Fig. 1b, the as-prepared CQDs have a narrow

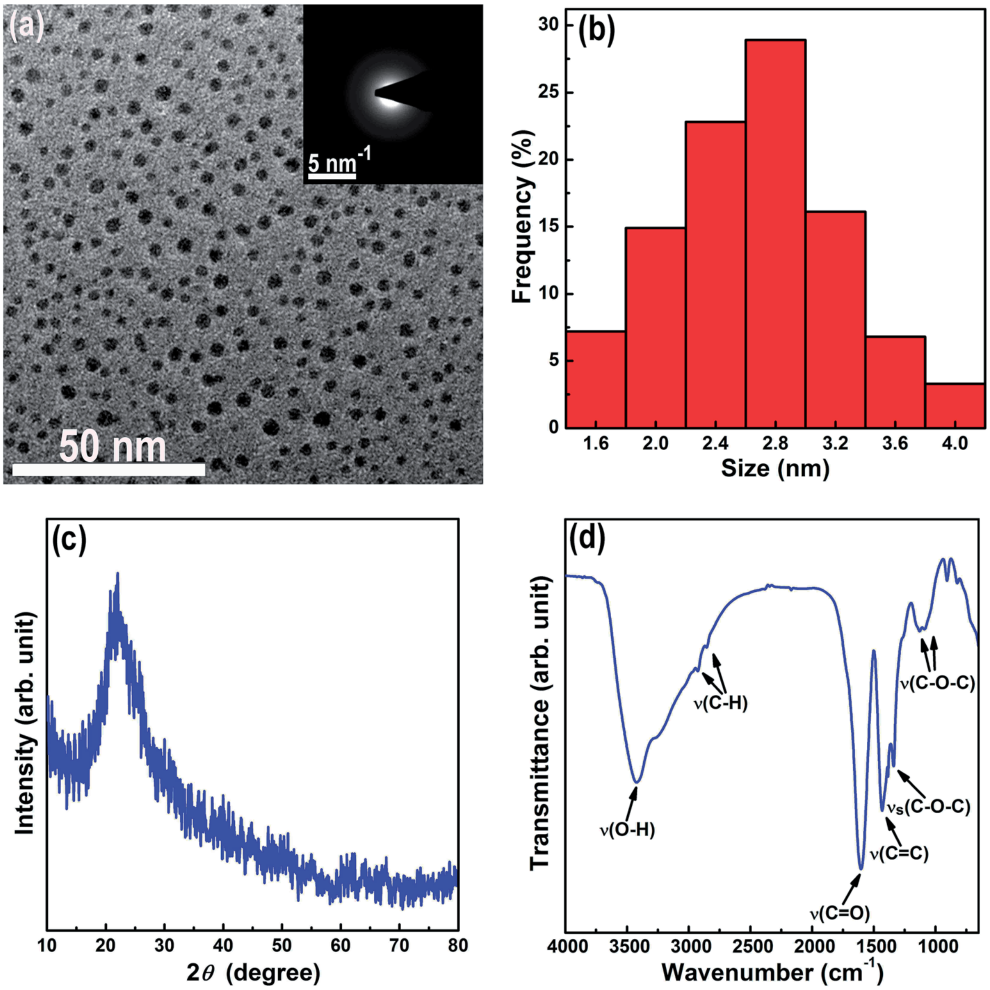

Fig. 1 TEM micrograph (the inset shows the SAED pattern) (a), size distribution histogram (b), XRD pattern (c), and FTIR spectrum (d) of the CQDs.

size distribution between 1.5 and 4.1 nm and an average particle size of 2.7 nm. The SAED pattern in the inset of Fig. 1a shows broad diffraction halos and a faint larger one, indicating that the as-prepared CQDs are amorphous in structure. The XRD pattern of the as-prepared CQDs in Fig. 1c shows only a single diffuse halo around 23.5° (2θ) which is indicative of amorphous structure. The FTIR spectrum of the as-prepared CQDs in Fig. 1d shows the distinct absorption bands of O–H at 3422 cm^{-1}, C–H at 2927 and 2855 cm^{-1}, C═O at 1605 cm^{-1}, C═C at 1433 cm^{-1}, C–O–C asymmetric stretching vibration at 1339 cm^{-1}, and C–O–C symmetric stretching vibration at 1129 and 1090 cm^{-1}.[33,34] The FTIR spectrum indicates the existence of OCFGs in the as-prepared CQDs. These OCFGs improve the hydrophilicity and stability of the CQDs in aqueous systems. Moreover, they help combine the CQDs with other nanomaterials because of the strong chemical interactions between the OCFGs on the CQDs and other nanomaterials.[35,36]

3.2 Characterizations of $SrTiO_3$ nanoparticles and CQD/$SrTiO_3$ nanocomposite

CQD/$SrTiO_3$ nanocomposite was prepared by combining the CQDs with $SrTiO_3$ nanoparticles through a simple impregnation process. The structure and composition of the prepared CQD/$SrTiO_3$ nanocomposite were analyzed by TEM, XRD, EDS, and XPS. The XRD patterns of the pure $SrTiO_3$ nanoparticles and CQD/$SrTiO_3$ nanocomposite (Fig. 2a) show the distinctive diffraction peaks of $SrTiO_3$ with the perovskite structure of a cubic symmetry (JCPDS no. 79-0176),[19] and no diffraction peaks from impurities such as TiO_2 or $Ti(OH)_4$ were detected. For the CQD/$SrTiO_3$ nanocomposite, a diffuse peak at 23.5° was observed and may be attributed to the small quantity of the CQDs in the CQD/$SrTiO_3$ nanocomposite.[37] The low magnification TEM image of the pure $SrTiO_3$ nanoparticles in Fig. 2b shows that the pure $SrTiO_3$ nanoparticles are slightly agglomerated and 20 to 40 nm in size. After the combination with the CQDs, the low magnification TEM image of the resulting CQD/$SrTiO_3$ nanocomposite nanoparticles in Fig. 2c reveals that the CQD/$SrTiO_3$ nanoparticles are agglomerated and almost same in size and morphology as the $SrTiO_3$ nanoparticles. This indicates that the introduction of the CQDs does not change the morphology and size of the $SrTiO_3$ nanoparticles significantly. Due to the presence of hydrophilic OCFGs on the CQD/$SrTiO_3$ nanocomposite nanoparticles, which will be confirmed by the XPS spectra, the agglomerates of the dry CQD/$SrTiO_3$ nanocomposite nanoparticles should be soft

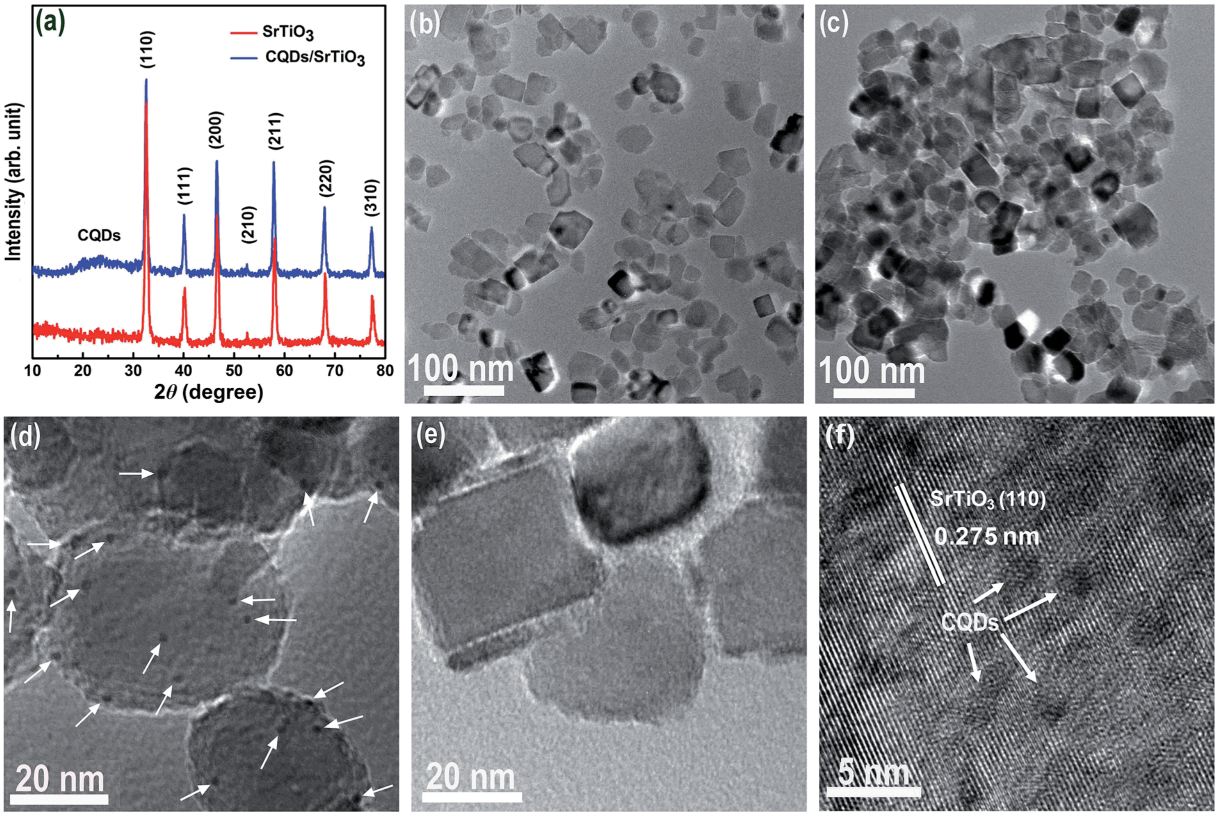

Fig. 2 XRD patterns (a) of pure $SrTiO_3$ and the CQD/$SrTiO_3$ nanocomposite and TEM or high-resolution TEM images of pure $SrTiO_3$ (b and e) and the CQD/$SrTiO_3$ nanocomposite (c, d, and f). The CQDs are marked with white arrows.

agglomeration. The high magnification TEM image of the CQD/$SrTiO_3$ nanocomposite in Fig. 2d reveals that a large number of fine nanoparticles (marked with white arrows) are attached to the surface of the $SrTiO_3$ nanoparticles. The high magnification TEM image of pure $SrTiO_3$ nanoparticles prepared in absolute ethanol in Fig. 2e shows the smooth surface of the pure $SrTiO_3$ nanoparticles. So the fine nanoparticles on the $SrTiO_3$ nanoparticles (Fig. 2d) should be the CQDs. This supports the formation of the CQD/$SrTiO_3$ nanocomposite by the addition of the CQDs. The high-resolution TEM image of the CQD/$SrTiO_3$ nanocomposite in Fig. 2f reveals lattice fringes of an $SrTiO_3$ nanoparticle and a large number of CQDs (marked with white arrows) attached onto the surface of an $SrTiO_3$ nanoparticle. A fringe spacing of 0.275 nm is in good agreement with the (200) interplanar spacing of $SrTiO_3$. The EDS element mappings in Fig. 3 clearly show that the C, O, Sr, and Ti elements are uniformly distributed in the nanocomposite, confirming that the CQD/$SrTiO_3$ nanocomposite consists of CQDs and $SrTiO_3$. The content of CQDs in the CQD/$SrTiO_3$ nanocomposite was estimated to be about 4.13 wt% by EDS analysis (Fig. S1 in ESI†). Such a structural feature suggests the combination of $SrTiO_3$ with CQDs which may endow the resulting nanocomposite with a good contact between CQDs and $SrTiO_3$. This is crucial to achieving a promoted interfacial charge transfer.

To analyze the interactions of the CQDs with $SrTiO_3$, XPS analysis was performed on the CQD/$SrTiO_3$ nanocomposite. The XPS spectrum (Fig. 4a) shows the existence of C, O, Sr, and Ti in the CQD/$SrTiO_3$ nanocomposite. The high-resolution XPS spectrum of Sr_{3d} in Fig. 4b contains two peaks at 132.4 and 134.2 eV which can be attributed to $Sr_{3d5/2}$ and $Sr_{3d3/2}$, respectively.[38] The high-resolution XPS spectrum of Ti_{2p} in Fig. 4c shows two peaks at 457.8 and 463.8 eV which are assigned to $Ti_{2p3/2}$ and $Ti_{2p1/2}$, respectively.[39] The high-resolution XPS spectrum of O_{1s} in Fig. 4d displays three peaks at 533.1, 531.8, and 529.4 eV which are assigned to C–O, C=O, and Ti–O, respectively.[39,40] The high-resolution C_{1s} XPS spectra of the CQD/$SrTiO_3$ nanocomposite and CQDs are shown in Fig. 4e and f, respectively. The XPS peaks of the C_{1s} spectrum centered at the binding energies of 288.5, 286.1, and 284.5 eV are attributed to C=O, C–O, and C–C/C=C, respectively.[40] A new peak at 281.5 eV in the C_{1s} spectrum of the CQD/$SrTiO_3$ nanocomposite appears compared to that of the CQDs. This new peak may be attributed to the chemical interaction between the CQDs and $SrTiO_3$ in the CQD/$SrTiO_3$ nanocomposite.[39,41] The XPS analysis results reveal the presence of CQDs in the CQD/$SrTiO_3$ and the strong interface interactions between CQDs and $SrTiO_3$.

3.3 Optical properties

Photoabsorption capability is an important factor influencing the photocatalytic performance of photocatalysts and usually evaluated from UV-vis diffuse reflectance spectrum.[42,43] As shown in Fig. 5a, the pure $SrTiO_3$ nanoparticles show strong absorption in the UV region which originates from the charge

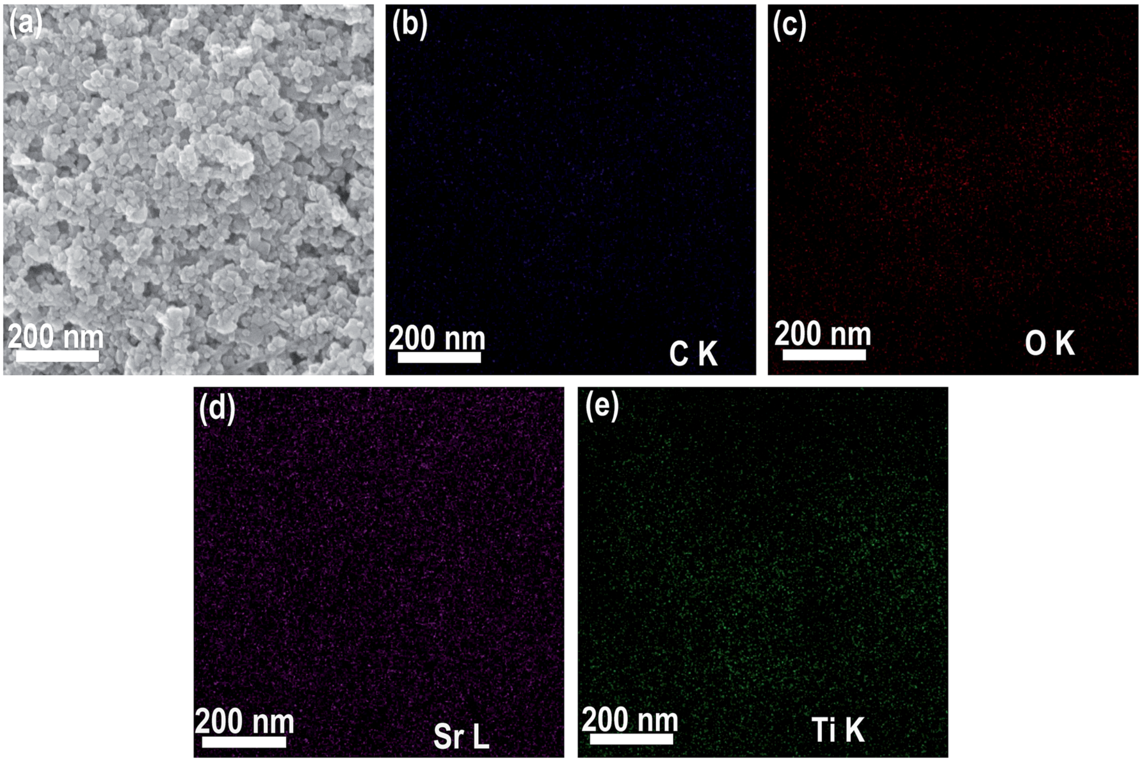

Fig. 3 SEM image of the CQD/$SrTiO_3$ nanocomposite (a) and corresponding elemental mapping images of C (b), O (c), Sr (d), and Ti (e).

transfer response of $SrTiO_3$ from the valence band (VB) to the conduction band (CB). Compared with pure $SrTiO_3$, the CQD/$SrTiO_3$ nanocomposite exhibits obvious visible light absorption ranging from 400 to 600 nm besides the strong UV absorption. The enhanced light absorption of the CQD/$SrTiO_3$ nanocomposite can be ascribed to the optical absorption of CQDs.[11,15,17] The optical band gaps of the pure $SrTiO_3$ and CQD/$SrTiO_3$ nanocomposite can be estimated *via* the formula $(\alpha h\nu)^n = A(h\nu - E_g)$, where α, h, ν, E_g, and A are the absorption coefficient, Planck constant, light frequency, band gap, and a constant, respectively, and n is an exponent determined by the nature of the electron transition during the absorption process ($n = 2$ for allowed direct transition and $n = 1/2$ for allowed indirect transition).[19,44,45] Fig. 5b shows a curve of $(\alpha h\nu)^2$ *versus* $h\nu$ from which the band gaps of $SrTiO_3$ and CQD/$SrTiO_3$ were estimated to be 3.16 and 3.15 eV, respectively. These results indicate that $SrTiO_3$ and CQD/$SrTiO_3$ have almost the same band gap energy within the experiment error. The band gap of $SrTiO_3$ was not narrowed by combining with CQDs. Similar results were reported in literature.[45,46] The UV-vis absorption spectrum of the CQDs in the range of 200–600 nm (Fig. S2 in ESI†) displays a broad absorption peak centered at 250 nm representing a typical absorption of an aromatic π system.[47] Reported studies showed that the upconverted emission of CQDs was responsible for the visible-light-responding photocatalytic performance of the CQD-based composite photocatalysts.[47,48] However, this is not the case of our present CQD/$SrTiO_3$ photocatalyst. As shown in Fig. 6, the upconverted emission wavelength of the CQDs is larger than 400 nm under excitation of different wavelengths. Therefore, upconverted emission of the CQDs is not effective to excite photocatalysis of $SrTiO_3$.

3.4 Photocatalytic performances

The photocatalytic performance of the CQD/$SrTiO_3$ nanocomposite was evaluated and compared with pure $SrTiO_3$ by the degradation of RhB under sunlight irradiation. The adsorption analysis of the catalysts in dark for RhB (Fig. S3 in ESI†) reveals that the absorption–desorption balance is achieved between the catalysts and RhB in about 30 min. About 10% and 11% of RhB was adsorbed in dark by $SrTiO_3$ and the CQD/$SrTiO_3$ nanocomposite, respectively, within about 30 min. This should be attributed to their different adsorption capacity. Fig. 7a plots the RhB concentration *versus* irradiation time under sunlight. RhB has about 7% self-degradation after irradiation for 120 min. When the CQDs were used as photocatalyst, the degradation of RhB is similar to the self-degradation of pure RhB. This manifests that the CQDs have almost no photocatalytic performance under sunlight. In contrast, the degradation of RhB in the presence of the CQD/$SrTiO_3$ nanocomposite under sunlight reaches 73% for 120 min whereas only 22% of RhB is degraded by using pure $SrTiO_3$. As well known, most of the photocatalytic reactions follow a pseudo-first-order kinetic equation, $-\ln(C/C_0) = kt$, where C_0 and C are the equilibrium concentration of adsorption and the concentration of RhB at the irradiation time t, respectively, and k is the apparent rate constant. Fig. 7b illustrates the pseudo-

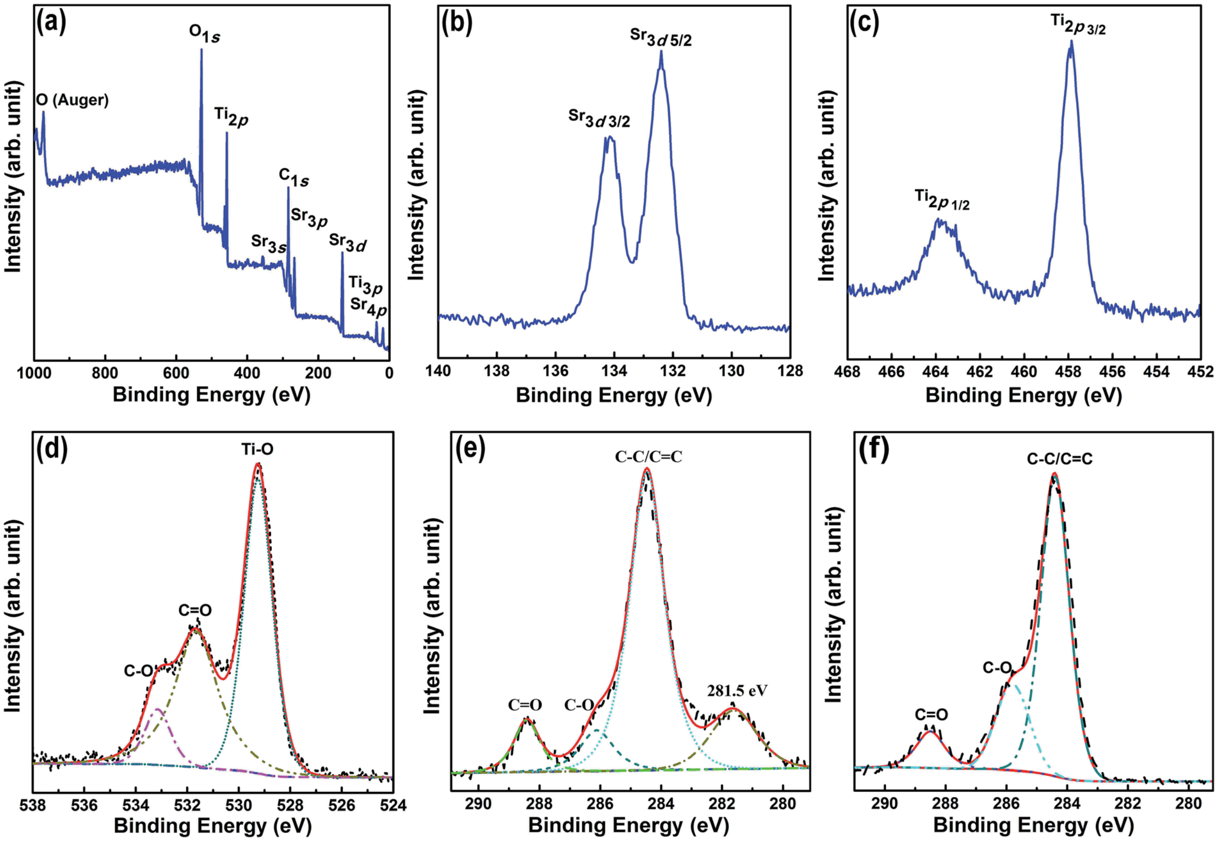

Fig. 4 XPS (a) and enlarged Sr_{3d} (b), Ti_{2p} (c), O_{1s} (d), and C_{1s} (e) spectra of the CQD/$SrTiO_3$ nanocomposite and enlarged C_{1s} spectrum of the CQDs (f).

first-order kinetics data for the photodegradation of RhB using pure $SrTiO_3$ and CQD/$SrTiO_3$ nanocomposite. The apparent rate constants are 0.01006 and 0.00183 min^{-1} for CQD/$SrTiO_3$ and $SrTiO_3$, respectively. The photocatalytic reaction rate of the CQD/$SrTiO_3$ nanocomposite is about 5.5 times as large as that of pure $SrTiO_3$. These results suggest that the excellent photocatalytic performance of the CQD/$SrTiO_3$ nanocomposite may be attributed to the interaction between the CQDs and $SrTiO_3$. In addition, the TOC analysis for the degradation of RhB by the CQD/$SrTiO_3$ nanocomposite (Fig. S4 in ESI†) shows that after an irradiation of 2 h, about 22% TOC removal is achieved, implying that RhB degradation is accompanied by partial mineralization.

3.5 Photocatalytic mechanism

In order to understand the enhanced photocatalytic performance of the CQD/$SrTiO_3$ nanocomposite, the photocatalytic mechanism of the CQD/$SrTiO_3$ nanocomposite was analyzed using the EIS and PL spectra. The EIS measurements were usually employed to evaluate the charge transfer resistance and

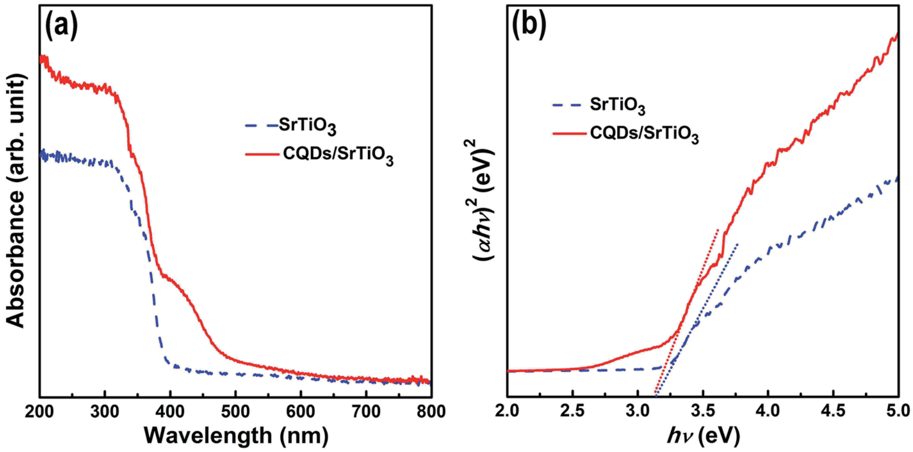

Fig. 5 UV-vis diffuse reflectance spectrum (a) and $(\alpha h\nu)^2$ *versus* $h\nu$ curve (b) of pure $SrTiO_3$ and the CQD/$SrTiO_3$ nanocomposite.

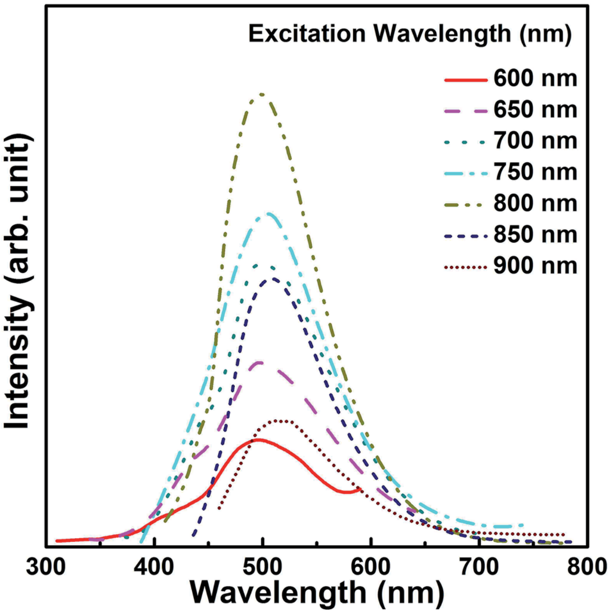

Fig. 6 Upconverted PL emission spectra of the CQDs at different excitation wavelengths.

the separation efficiency of the photogenerated e$^-$–h$^+$ pairs.[49] In the presence of CQDs, the CQD/SrTiO$_3$ nanocomposite exhibits much lower charge transfer resistance than the pure SrTiO$_3$ which is verified by the significantly reduced diameter of the Nyquist circle in the high frequency region of the EIS patterns shown in Fig. 8a. This clearly indicates that a faster interfacial charge transfer to the electron acceptor occurs and results in an effective separation of the e$^-$–h$^+$ pairs by the introduction of CQDs.[50] This would enhance the photocatalytic performance. The CQDs may act as electron acceptor for suppressing charge recombination. In order to further confirm this mechanism, PL spectra of SrTiO$_3$ and the CQD/SrTiO$_3$ nanocomposite were comparatively analyzed. Because the PL emission mainly results from the recombination of free charge carriers, PL is an effective tool to analyze the transfer and recombination processes of photogenerated charge carriers in SrTiO$_3$ and the CQD/SrTiO$_3$ nanocomposite.[51] The higher the PL intensity, the greater the probability of the charge carrier recombination.[52] The comparison of the PL spectra of pure SrTiO$_3$ and the CQD/SrTiO$_3$ nanocomposite is shown in Fig. 8b. The PL emission intensity of the CQD/SrTiO$_3$ nanocomposite is much lower than that of pure SrTiO$_3$. This indicates that the recombination of the photogenerated e$^-$–h$^+$ pairs is strongly suppressed by the attachment of the CQDs to the SrTiO$_3$ nanoparticles. In other words, photogenerated electrons (e$^-$) in excited SrTiO$_3$ nanoparticles may be injected into the CQDs. This PL analysis result is consistent with the above EIS analysis, which confirms that CQDs can accept the photogenerated e$^-$ from SrTiO$_3$ and promote the efficient separation of photogenerated e$^-$–h$^+$ pairs.[9,13]

In order to more deeply understand the photodegradation mechanism of the CQD/SrTiO$_3$ nanocomposite, the VB and CB edge potentials of SrTiO$_3$ were estimated according to the equations $E_{VB} = X - E^e + 0.5\ E_g$ and $E_{CB} = E_{VB} - E_g$, where X is the electronegativity of the semiconductor, 4.94 eV for SrTiO$_3$,[53] E^e the energy of free electrons on the hydrogen scale (about 4.5 eV), and E_g the band gap energy of the semiconductor, 3.16 eV for SrTiO$_3$ (Fig. 5). E_{VB} of SrTiO$_3$ was determined to be 2.02 eV. E_{CB} of SrTiO$_3$ was estimated to be −1.14 eV *versus* normal hydrogen electrode (NHE). The VB potential of SrTiO$_3$ (2.02 eV) is less positive than E^0 ($^\bullet$OH/OH$^-$) (2.38 eV *vs.* NHE),[54] implying that OH$^-$ cannot be oxidized to yield $^\bullet$OH by h_{VB}^+ of SrTiO$_3$. However, the CB potential of SrTiO$_3$ (−1.14 eV) is much less positive than E^0 (O$_2$/$^\bullet$O$_2^-$) (−0.046 eV *vs.* NHE),[55] implying that the photogenerated e$^-$ in the CB can reduce O$_2$ to generate $^\bullet$O$_2^-$. h$^+$ in the VB of SrTiO$_3$ can directly oxidize RhB.[56,57] The above analysis indicates that h$^+$ and $^\bullet$O$_2^-$ play an important role in the photodegradation process and $^\bullet$OH is not a main reactive species in the photodegradation.

On the basis of the above experimental results, a possible photocatalytic mechanism for the CQD/SrTiO$_3$ nanocomposite is schematically depicted in Fig. 9. When SrTiO$_3$ is irradiated by sunlight, electrons (e$^-$) can be excited from the VB into the CB

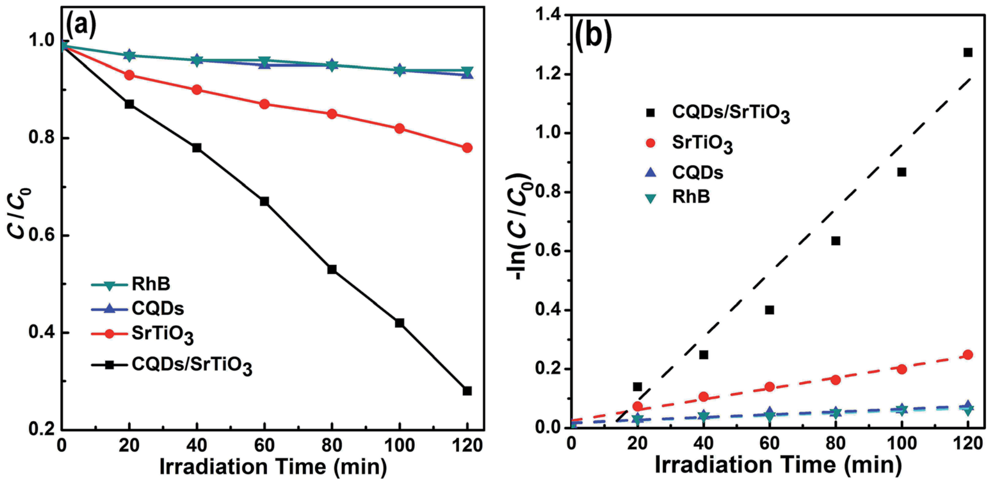

Fig. 7 Photocatalytic degradation of RhB by pure SrTiO$_3$ and CQD/SrTiO$_3$ nanocomposite under sunlight irradiation (a) and the corresponding pseudo-first-order kinetics plot for pure SrTiO$_3$ and CQD/SrTiO$_3$ nanocomposite (b).

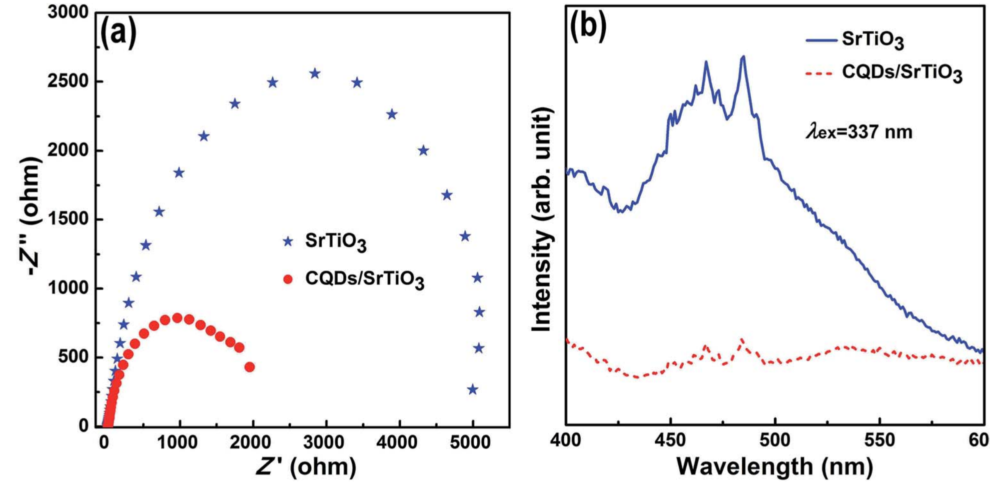

Fig. 8 EIS (a) and room temperature PL (b) spectra of pure $SrTiO_3$ and the CQD/$SrTiO_3$ nanocomposite.

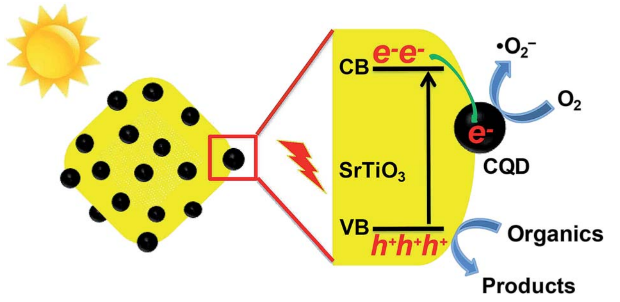

Fig. 9 Schematic of a possible photocatalytic mechanism for the CQD/$SrTiO_3$ nanocomposite under sunlight irradiation.

of $SrTiO_3$ remaining holes (h^+) in the VB. Generally, most of the photogenerated e^-–h^+ pairs quickly recombine and only a small fraction of e^- and h^+ participates in the photocatalytic reaction. However, when the $SrTiO_3$ nanoparticles is combined with the CQDs to form the CQD/$SrTiO_3$ nanocomposite, the photogenerated e^- in the CB of $SrTiO_3$ tend to transfer to the CQDs due to the excellent electron transfer and reservoir properties of the CQDs.[2,9] These e^- can be shuttled in the special conducting network of the CQDs,[58] retarding the recombination of photogenerated e^-–h^+ pairs at the junction interface. Most e^- would accumulate in the CQDs and then combine with O_2 to form $^{\bullet}O_2^-$. The longer-lived h^+ in the VB of $SrTiO_3$ can oxidize RhB. So the RhB solution was degraded by the photogenerated h^+ and $^{\bullet}O_2^-$.[56,57] Therefore, the introduction of the CQDs (electron acceptor) to the $SrTiO_3$ nanoparticles will facilitate the efficient separation of photogenerated e^-–h^+ pairs and thus enhance the photocatalytic performance.

4. Conclusions

A modified acidic oxidation process for the preparation of CQDs from activated carbon was developed by direct evaporation of the residual acid. Using this process, disperse fine spherical amorphous CQDs with an average particle size of 2.7 nm were prepared. The as-prepared CQDs with OCFGs endow them excellent hydrophilicity, facilitating further functionalization and applications. A novel photocatalyst (CQD/$SrTiO_3$) was fabricated by combining the as-prepared CQDs with $SrTiO_3$ nanoparticles through a simple impregnation process. The photocatalytic reaction rate of the CQD/$SrTiO_3$ nanocomposite is about 5.5 as large as that of the pure $SrTiO_3$ nanoparticles in the degradation of RhB under sunlight. The significant enhancement of photocatalytic performance may be ascribed to the improved charge separation efficiency resulted from the presence of CQDs. RhB is degraded by the photogenerated h^+ and $^{\bullet}O_2^-$ reduced by the photogenerated e^-. This work may open a door to the development of new CQD-based photocatalytic nanocomposites.

Conflicts of interest

There are no conflicts of interest to declare.

Acknowledgements

This work was supported by the National Natural Science Foundation of China (51272098, 51551201, and 51772137).

References

1 S. N. Baker and G. A. Baker, *Angewandte Chemie*, 2010, **49**, 6726–6744.
2 H. Li, Z. Kang, Y. Liu and S. T. Lee, *J. Mater. Chem.*, 2012, **22**, 24230–24253.
3 F. Yuan, S. Li, Z. Fan, X. Meng, L. Fan and S. Yang, *Nano Today*, 2016, **11**, 565–586.
4 S. Zhu, Q. Meng, L. Wang, J. Zhang, Y. Song, H. Jin, K. Zhang, H. Sun, H. Wang and B. Yang, *Angewandte Chemie*, 2013, **52**, 3953–3957.
5 Y. Guo, Y. Chen, F. Cao, L. Wang, Z. Wang and Y. Leng, *RSC Adv.*, 2017, **7**, 48386–48393.
6 Y. Song, W. Shi, W. Chen, X. Li and H. Ma, *J. Mater. Chem.*, 2012, **22**, 12568–12573.

7 X. Zhang, C. Liu, Z. Li, J. Guo, L. Shen, W. Guo, L. Zhang, S. Ruan and Y. Long, *Chem. Eng. J.*, 2017, **315**, 621–629.

8 M. Zhang, Z. Fang, X. Zhao, Y. Niu, J. Lou, L. Zhao, Y. Wu, S. Zou, F. Du and Q. Shao, *RSC Adv.*, 2016, **6**, 104979–104984.

9 J. Di, J. Xia, Y. Ge, H. Li, H. Ji, H. Xu, Q. Zhang, H. Li and M. Li, *Appl. Catal., B*, 2015, **168–169**, 51–61.

10 C. Huang, Y. Hong, X. Yan, L. Xiao, K. Huang, W. Gu, K. Liu and W. Shi, *RSC Adv.*, 2016, **6**, 40137–40146.

11 B. Song, T. Wang, H. Sun, Q. Shao, J. Zhao, K. Song, L. Hao, L. Wang and Z. Guo, *Dalton Trans.*, 2017, **46**, 15769–15777.

12 J. Di, J. Xia, Y. Huang, M. Ji, W. Fan, Z. Chen and H. Li, *Chem. Eng. J.*, 2016, **302**, 334–343.

13 H. Zhang, H. Huang, H. Ming, H. Li, L. Zhang, Y. Liu and Z. Kang, *J. Mater. Chem.*, 2012, **22**, 10501–10506.

14 D. Tang, H. Zhang, H. Huang, R. Liu, Y. Han, Y. Liu, C. Tong and Z. Kang, *Dalton Trans.*, 2013, **42**, 6285–6289.

15 J. Di, J. Xia, M. Ji, H. Li, H. Xu, H. Li and R. Chen, *Nanoscale*, 2015, **7**, 11433–11443.

16 H. Zhang, H. Ming, S. Lian, H. Huang, H. Li, L. Zhang, Y. Liu, Z. Kang and S. T. Lee, *Dalton Trans.*, 2011, **40**, 10822–10825.

17 X. Yu, J. Liu, Y. Yu, S. Zuo and B. Li, *Carbon*, 2014, **68**, 718–724.

18 H. W. Kang, S. N. Lim and S. B. Park, *Int. J. Hydrogen Energy*, 2012, **37**, 5540–5549.

19 S. Tonda, S. Kumar, O. Anjaneyulu and V. Shanke, *Phys. Chem. Chem. Phys.*, 2014, **16**, 23819–23828.

20 L. Mu, Y. Zhao, A. Li, S. Wang, Z. Wang, J. Yang, Y. Wang, T. Liu, R. Chen, J. Zhu, F. Fan, R. Li and C. Li, *Energy Environ. Sci.*, 2016, **9**, 2463–2469.

21 H. Tan, Z. Zhao, W. Zhu, E. N. Coker, B. Li, M. Zheng, W. Yu, H. Fan and Z. Sun, *ACS Appl. Mater. Interfaces*, 2014, **6**, 19184–19190.

22 H. Peng and J. Travas-Sejdic, *Chem. Mater.*, 2009, **21**, 5563–5565.

23 H. Li, X. He, Y. Liu, H. Huang, S. Lian, S. T. Lee and Z. Kang, *Carbon*, 2011, **49**, 605–609.

24 H. Zhu, X. Wang, Y. Li, Z. Wang, F. Yang and X. Yan, *Chem. Commun.*, 2009, **34**, 5118–5120.

25 J. Lu, J. Yang, J. Wang, A. Lim, S. Wang and K. P. Loh, *ACS Nano*, 2009, **3**, 2367–2375.

26 S. Hu, J. Liu, J. Yang, Y. Wang and S. Cao, *J. Nanopart. Res.*, 2011, **13**, 7247–7252.

27 Y. Deng, D. Zhao, X. Chen, F. Wang, H. Song and D. Shen, *Chem. Commun.*, 2013, **49**, 5751–5753.

28 Z. C. Yang, M. Wang, A. M. Yong, S. Y. Wong, X. H. Zhang, H. Tan, A. Y. Chang, X. Li and J. Wang, *Chem. Commun.*, 2011, **47**, 11615–11617.

29 J. Wang, C. F. Wang and S. Chen, *Angewandte Chemie*, 2012, **124**, 9431–9435.

30 L. Wang, X. Chen, Y. Lu, C. Liu and W. Yang, *Carbon*, 2015, **94**, 472–478.

31 M. Wu, Y. Wang, W. Wu, C. Hu, X. Wang, J. Zheng, Z. Li, B. Jiang and J. Qiu, *Carbon*, 2014, **78**, 480–489.

32 Y. Su, M. Xie, X. Lu, H. Wei, H. Geng, Z. Yang and Y. Zhang, *RSC Adv.*, 2014, **4**, 4839–4842.

33 H. Zhu, X. Wang, Y. Li, Z. Wang, F. Yang and X. Yang, *Chem. Commun.*, 2009, **34**, 5118–5120.

34 Y. Liu, Y. Liu, S. J. Park, Y. Zhang, T. Kim, S. Chae, M. Park and H. Y. Kim, *J. Mater. Chem. A*, 2015, **3**, 17747–17754.

35 H. Wang, J. T. Robinson, G. Diankov and H. Dai, *J. Am. Chem. Soc.*, 2010, **132**, 3270–3271.

36 Y. Zhu, X. Ji, C. Pan, Q. Sun, W. Song, L. Fang, Q. Chen and C. E. Banks, *Energy Environ. Sci.*, 2013, **6**, 3665–3675.

37 H. Bozetine, Q. Wang, A. Barras, M. Li, T. Hadjersi, S. Szunerits and R. Boukherrou, *J. Colloid Interface Sci.*, 2016, **465**, 286–294.

38 S. Fuentes, P. Muñoz, N. Barraza, E. Chávez-Ángel and C. M. S. Torres, *J. Sol-Gel Sci. Technol.*, 2015, **75**, 593–601.

39 Y. Zhang, Z. Zhao, J. Chen, L. Cheng, J. Chang, W. Sheng, C. Hu and S. Cao, *Appl. Catal., B*, 2015, **165**, 715–722.

40 Y. Hu, J. Yang, L. Jia and J. S. Yu, *Carbon*, 2015, **93**, 999–1007.

41 B. Liu, Y. Huang, Y. Wen, L. Du, W. Zeng, Y. Shi, F. Zhang, G. Zhu, X. Xu and Y. Wang, *J. Mater. Chem.*, 2012, **22**, 7484–7491.

42 W. Li, X. Jia, P. Li, B. Zhang, H. Zhang, W. Geng and Q. Zhang, *ACS Sustainable Chem. Eng.*, 2015, **3**, 1101–1110.

43 H. Li, T. Hu, J. Liu, S. Song, N. Du, R. Zhang and W. Hou, *Appl. Catal., B*, 2016, **182**, 431–438.

44 G. Panomsuwan, O. Takai and N. Saito, *Phys. Status Solidi A*, 2013, **210**, 311–319.

45 J. Liu, Y. Liu, N. Liu, Y. Han, X. Zhang, H. Huang, Y. Lifshitz, S. T. Lee, J. Zhong and Z. Kang, *Science*, 2015, **347**, 970–974.

46 Y. Q. Zhang, D. K. Ma, Y. G. Zhang, W. Chen and S. M. Huang, *Nano Energy*, 2013, **2**, 545–552.

47 H. Li, X. He, Z. Kang, H. Huang, Y. Liu, J. Liu, S. Lian, C. H. A. Tsang, X. Yang and S. T. Lee, *Angewandte Chemie*, 2010, **49**, 4430–4434.

48 S. Zhuo, M. Shao and S. T. Lee, *ACS Nano*, 2012, **6**, 1059–1064.

49 D. Wang, X. Li, J. Chen and X. Tao, *Chem. Eng. J.*, 2012, **198–199**, 547–554.

50 X. Cao, G. Tian, Y. Chen, J. Zhou, W. Zhou, C. Tian and H. Fu, *J. Mater. Chem. A*, 2014, **2**, 4366–4374.

51 C. Zhao, W. Li, Y. Liang, Y. Tian and Q. Zhang, *Appl. Catal., A*, 2016, **527**, 127–136.

52 Z. Zhang, W. Wang, L. Wang and S. Sun, *ACS Appl. Mater. Interfaces*, 2012, **4**, 593–597.

53 J. Zhou, L. Yin, H. Li, Z. Liu, J. Wang, K. Duan, S. Qu, J. Weng and B. Feng, *Mater. Sci. Semicond. Process.*, 2015, **40**, 107–116.

54 J. Di, J. Xia, Y. Ge, L. Xu, H. Xu, M. He, Q. Zhang and H. Li, *J. Mater. Chem. A*, 2014, **2**, 15864–15874.

55 L. Ye, J. Chen, L. Tian, J. Liu, T. Peng, K. Deng and L. Zan, *Appl. Catal., B*, 2013, **130–131**, 1–7.

56 Q. X. Zeng, G. C. Xu, L. Zhang, H. Lin, Y. Lv and D. Z. Jia, *New J. Chem.*, 2018, **42**, 7016–7024.

57 L. Shi, L. Liang, J. Ma, F. Wang and J. Sun, *Catal. Sci. Technol.*, 2014, **4**, 758–765.

58 R. Wang, K. Q. Lu, Z. R. Tang and Y. J. Xu, *J. Mater. Chem. A*, 2017, **5**, 3717–3734.